Automatic Force-Based Probe Positioning for Precise Robotic Ultrasound Acquisition

Zhongliang Jiang[1], Matthias Grimm[1], Mingchuan Zhou[1], Ying Hu[2], Javier Esteban[1], Nassir Navab[1,3],

***Abstract*—The correct orientation of an ultrasound (US) probe is one of the main parameters governing the US image quality. With the rise of robotic ultrasound systems (RUSS), methods that can automatically compute the orientation promise repeatable, automatic acquisition from predefined angles resulting in high-quality US imaging. In the present paper, we propose a method to automatically position a US probe orthogonally to the tissue surface, thereby improving sound propagation and enabling RUSS to reach predefined orientations relatively to the surface normal at the contact point. The method relies on the derivation of the underlying mechanical model. Two rotations around orthogonal axes are carried out, while the contact force is being recorded. Then, the force data are fed into the model to estimate the normal direction. Accordingly, the probe orientation can be computed without requiring visual features. The method is applicable to the convex and linear probes. It has been evaluated on a phantom with varying tilt angles and on multiple human tissues (forearm, upper arm, lower back, and leg). As a result, it has outperformed existing methods in terms of accuracy. The mean ($\pm$SD) absolute angular difference on the in-vivo tissues averaged over all anatomies and probe types is $2.9\pm1.6^\circ$ and $2.2\pm1.5^\circ$ on the phantom.**

***Index Terms*—Medical robotics, robotic ultrasound, normal direction detection, parameters optimization**

I. Introduction

The importance of orthopedic surgery amplifies with an increase in life expectancy, as elderly people are more prone to bone-related injuries [1]. For example, 18% of elderly people and 25% of children in the USA suffer from distal radius fracture [1], [2]. The ultrasound (US) image is widely used in scanning bones and many other clinical applications owing to its low cost, high accessibility, and absence of ionizing radiation. For example, in 2017, over 9.2 million US scans were performed in England, which is twice and three times larger than the number of computer tomography (CT) scans and magnetic resonance imaging (MRI), respectively, during the same period [3].

To optimize the outcome of an orthopedic surgery, surgical navigation has been widely implemented in current clinical practice. To enable accurate navigation, it is necessary to perform a registration providing the consistency between the intra-operative US scans and the high resolution pre-operative scans, such as MRI or CT [4], [5]. Concerning orthopedic surgery, the bone surface is often considered to perform such a registration, as it has strong resistance to deformation [5]. Therefore, it is crucial to obtain high-quality US bone imaging. However, US examinations are highly operator-dependent, as it is challenging to exactly maintain or replicate acquisition parameters (the contact force and relative orientation between a probe and a tested object), even for experienced sonographers [6].

To address this challenge, the robotic-based techniques have been introduced to assist in US scanning owing to their high accuracy and reproducibility [7]–[9]. Applying the robotic US systems (RUSS) allows obtaining US sweeps with a repeatable predefined contact force and probe orientation (namely, the tilt angle θ_t between the probe center line and the normal direction of a scanned tissue), which are the two most important parameters governing the US image quality. Huang *et al.* employed two strain sensing elements attached onto both sides of the probe front surface to monitor the pressure between a probe and a subject [10]. To reconstruct 3D US arteries, Pierrot *et al.* implemented an external force control scheme aiming to exert a given effort on skin based on a force/torque (F/T) sensor mounted to the flange of a 7-DOF (degree of freedom) robotic arm [11]. Gilbertson *et al.* designed a 1-DOF hand-held device to perform freehand US scanning, while the predefined contact force was maintained using a hybrid position/force control scheme [6].

Pujas *et al.* showed that external control is able to reach a similar performance as the hybrid scheme for real implementations [12]. However, the implementation of an external force controller was deemed simpler compared with a hybrid controller used in industrial applications in [13]. Furthermore, the external control is particularly well-suited in the case when safety is of concern, as the acting position loop of external control could mitigate the disturbance occurred on the robotic arm. However, the performance of the classic hybrid method [13] is limited due to dynamic instability caused by the robot's dynamic model. Since we only require force control for one Cartesian direction (along probe), the spring-like external force controller [14] is employed to maintain a constant contact force in this study.

However, in addition to the contact force, the relative tilt angle θ_t is also crucial to fully parameterize a US scan, specifically when repeated US scans are required to monitor the changes in the anatomies of interest. To investigate the

Manuscript received Feb 26, 2020; revised Jun 22, 2020, Aug 19, 2020 and Sep 25, 2020; accepted Oct 21, 2020. (*Corresponding author:* Mingchuan Zhou.)

Zhongliang Jiang, Matthias Grimm, Mingchuan Zhou, Javier Esteban and Nassir Navab are with Computer Aided Medical Procedures, Technical University of Munich, Boltzmannstr. 3, 85748 Garching bei Munchen, Germany. (zl.jiang@tum.de)

Ying Hu is with Shenzhen Institutes of Advanced Technology, Chinese Academy of Sciences, Shenzhen 518055, China.

Nassir Navab is with Johns Hopkins University, Baltimore, USA.

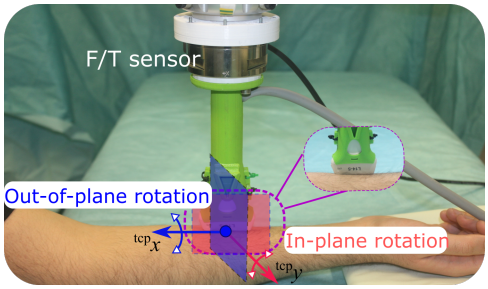

Fig. 1. Two rotations executed to optimize the probe orientation.

influence of θ_t, Hnatsenka *et al.* found that better quality could be obtained when θ_t is close to zero (the probe center line is situated close to the normal direction of the contact surface) [15]. This phenomenon is further aggravated in orthopedic applications, as the intensity reflection coefficient for most interfaces from soft tissues to bones are approximately 25% while that for most interfaces from soft tissues to soft tissues are less than 0.01% [16]. Therefore, it is reasonable to place the probe along the normal direction of unknown constraints for general US applications. Moreover, the probe is able to be further deflected from the normal direction by an explicit θ_t for specific applications, such as imaging the anatomies covered by ribs.

Some industrial applications, such as robotic polishing, also require to orient a tool attached to the flange along the normal direction of the constraint surface or a given direction θ_t. However, the constrained surface is usually known in industrial applications, such as mold manufacturing. Therefore, the desired posture of attached tools can be directly generated from CAD/CAM software for polishing a freeform surface [17]–[19]. Concerning an unknown constraint surface, Merlet *et al.* and Kazanzides *et al.* proposed using reaction force to determine the surface normal [20], [21]. However the estimation accuracy cannot be guaranteed when the surface is non-rigid. In addition, Yoshikawa *et al.* suggested moving the tool on the surface using a hybrid position/force control, and then, the normal direction was approximated according to the direction that is perpendicular to the line connecting two nearby positions on a considered trajectory [13]. However, this method requires a change of the contact point on the constraint surface.

To orient a US probe close to the normal direction of an unknown constraint surface for US applications, Chatelain *et al.* employed a visual servoing technique for a 3D US probe in [22]. However, for 2D probes which are much more common in clinical practice, the method is only able to optimize the in-plane orientation while the out-of-plane part still required to be adjusted via telemanipulation [23]. Huang *et al.* approximated the normal direction of the constraint surface considering the normal direction of a triangle composed by three neighbor points around the planned path on an image obtained by a depth camera prior to US scanning [24]. However, the surface obtained before the probe makes contact with the tissue can not adapt to deformations induced by the contact. Furthermore, the method's accuracy is limited by the employed hand-eye calibration and potential occlusions between the camera and the scanned tissue.

To build a RUSS independent of additional devices, Jiang *et al.* proposed an algorithm to identify the normal direction based on live US scans together with contact force values estimated from joint torques [25]. However, the accuracy of estimated force is highly depends on the joint configuration and accuracy of torque sensors in all joints of the robot. In addition, their computer vision based in-plane adjustment is limited to convex probes and requires the presence of sufficient amounts of shadows in a US scan. This limits the possibility of realizing potential clinical applications, as the preferred type of probes for limbs or carotid artery is linear.

This study aims to present a model based orientation optimization method to accurately place the probe perpendicular to the tissue surface for automatic RUSS. Accurately orienting the US probe to anatomies is an important step towards fully automatic RUSS with high-quality US imaging. This will further extend the usability of US modality for monitoring changes of tissues or lesions of interest, since it can provide accurate and repeatable probe orientation making scans easily comparable. To this end, we first build the mechanical model describing the reaction force during two rotations around a given contact point. Then the parameters of the derived model are optimized using particle swarm optimization (PSO) on the force data measured from an external F/T sensor. In addition, we show that the probe orientation is an important factor governing the image quality of orthopedic US scans. The effect of probe orientation θ_t on the orthopedic US image quality has been quantitatively investigated using a state-of-the-art US bone detection algorithm [5]. The desired normal is decomposed into two parts: an in-plane component $\mathbf{N}_i$ (co-planar with the US image plane) and an out-of-plane component $\mathbf{N}_o$ (orthogonal to the US image plane). These two components are estimated separately by executing two rotations around the corresponding axes, as shown in Fig. 1. Moreover, we report the results of experiments performed on both phantom and different human tissues. These results show that the proposed method outperforms existing approaches in terms of accuracy, and it is applicable in real conditions.

This paper is organized as follows. Section II provides the results of investigating the impact of the probe orientation on US bone detection. Section III presents the mechanical model for the in-plane and out-of-plane rotation. Section IV describes the denoising and optimization procedures used to extract the normal direction from the measured force values. Experimental validation on both phantom and in-vivo tissues with different probes are presented in Section V.

II. Effect of Probe Orientation on Bone Detection

A. Ultrasound Bone Detection

The bone surface detection method by Salehi *et al.* [5] is used for bone detection in this paper. The method is based on a convolutional neural network to first segment the bone in the US scans. Then the segmentations are post-processed to extract the bone surface. The model was trained using US acquisitions

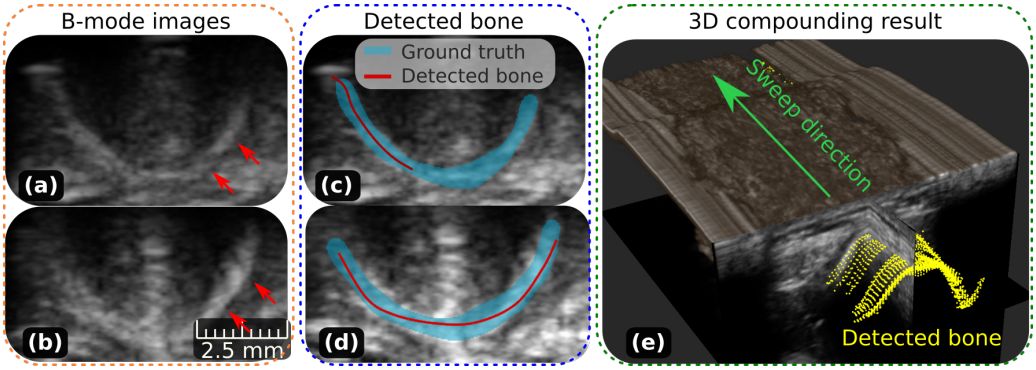

Fig. 2. Bone detection results for an US sweep of the radius bone for various probe orientations. (a) and (b) are the B-mode US slices from two sweeps of a volunteer's radius bone when the probe is placed in a tilted ($\theta_t = 15°$) and normal orientation ($\theta_t = 0°$). (c) and (d) show the corresponding bone detection results. (e) shows the compounded volume with the detected bone surface on each slice of the sweep for $\theta_t = 0°$.

from multiple subjects using different acquisition settings. The method is shown to outperform existing feature-based methods both in terms of precision and recall. The method with trained model was thankfully obtained from the authors implemented in ImFusionSuite (ImFusion GmbH, Munich, Germany).

The results of applying the method to an US sweep performed on an in-vivo radius bone is shown in Fig. 2. As it can be seen in Fig. 2, the US image acquired with $\theta_t = 0°$ is more contrast compared with the scan from the other sweep with the tilted ($\theta_t = 15°$) probe orientation (brighter than the surrounded soft tissues as denoted by red arrows). Hence, the corresponding detection result for $\theta_t = 0°$ is much better. Since bones are acoustically in-homogeneous, the US waves are scattered away rather than reflected back to the probe if θ_t is not zero [26]. When increasing θ_t the ability of a US probe to properly contact the scanned surface deteriorates due to the high stiffness of a bone, which further degrades image quality.

To quantitatively assess the quality of bone detection, the detected bone feature coefficient (DBFC) λ_c is considered. Intuitively, λ_c describes the true positive rate adapted to the case where the detection is confined to a curve, whereas the annotation is volumetric. It is computed by dividing the number of the true positive detected pixels over the difference in the column indeces between the leftmost and rightmost annotated pixels. A larger λ_c means to a larger true positive rate, which benefits a potential registration. This is shown in Eq. (1).

$$\lambda_c = \frac{|\Omega|}{G_r - G_l} \quad \text{where } \Omega = \{p | p \in \mathbf{DET} \cap \mathbf{GT}\} \qquad (1)$$

where G_l and G_r represent the column index of the leftmost and rightmost pixels of the ground truth; **DET** and **GT** represent the sets containing all pixels belonging to the detected bone surface (line) and the labelled ground truth (area) and Ω is the intersection of **DET** and **GT**.

B. Detection Quality with Different Probe Orientations

To investigate the impact of θ_t on the US imaging quality and bone detection results, five US sweeps (each includes 195 2D B-mode scans) on the volunteer's forearm with different θ_t ($0°$, $5°$, $10°$, $15°$, and $20°$) were obtained using a linear US probe. The forearm surface is seen as flat during short sweeps ($50\ mm$). To ensure the constant contact force F_c, all sweeps were recorded using the compliant control scheme described in [14]. Furthermore, to ensure that the imaged area is the same despite the varying tilt angles, only the middle part of each sweep is considered. The bone detection results for the five sweeps are represented in Fig. 3.

The sweep recorded under the normal direction ($\theta_t = 0°$) contains more B-mode scans (70%) with $\lambda_c \geq 0.75$ compared with the sweeps corresponding to the other four directions. It could be seen that the second highest peak in that bin corresponds to the θ_t of $10°$. However, when considering the neighbor bin ($\lambda_c \in [0.5, 0.75)$), the sweep with $\theta_c = 5°$ contains 73% of scans with $\lambda_c \geq 0.5$, whereas the sweep with $\theta_c = 10°$ contains only 66%. Regarding sweeps with $\lambda_c < 0.25$, the sweeps with θ_t of $0°$ and $5°$ comprised only 6% and 3%, respectively. With an increase in θ_t to $20°$, the amount of sweeps with $\lambda_c < 0.25$ augmented to 18%, 34%, and 29% for θ_t of $10°$, $15°$, and $20°$, respectively. Hence it can be seen that the bone detection quality of the state-of-the-art US bone detection method improves, as the US probe is oriented closer to the normal direction.

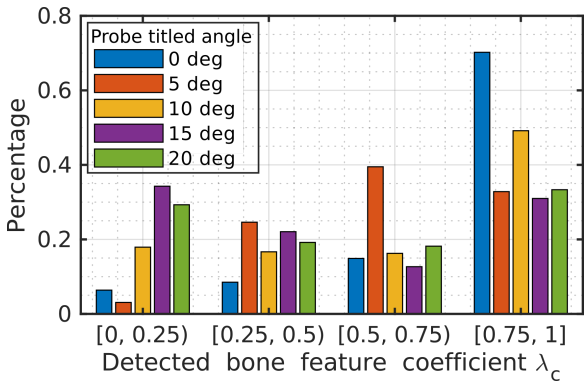

Fig. 3. Bone detection results for US sweeps obtained from a volunteer's forearm using a linear US probe. The probe was tilted in various angles. The contact force is $5\ N$.

III. Normal Direction Detection

A. Strategy for Searching the Normal Direction

To ensure the imaging quality and patient safety, the compliant control scheme described in Section IV-A is employed to maintain a constant force F_c along the probe center line $\mathbf{C}$ during US scans (see Fig. 4). The target tissues in orthopedic applications (i.e. limbs) are rigid due to the presence of bones, whose elastic modulus is more than $8.91\ Gpa$ [27]. Thus, when a constant F_c is exerted along the probe, reaction force $\mathbf{F}_r$ is generated along $\mathbf{N}$ of the constraint surface to balance F_c. The other reaction force component normal to F_c varies according to the change in the relative posture between probe $\mathbf{C}$ and unknown $\mathbf{N}$ as shown in Fig. 4 (d). According to the concept of reaction force defined in theoretical mechanics, it can be inferred that when an external force (F_c) is applied along the normal direction of a contact surface ($\mathbf{N}$), the resulting reaction force components in the other two orthogonal directions should be zero.

To estimate $\mathbf{N}$ of an unknown constraint surface, two rotations with a given point of contact around two orthogonal axes (x_{sa} and y_{sa}) are executed. During the process of rotating, the reaction force component ${}^{sa}F_y$ and ${}^{sa'}F_x$ (see Fig. 4 (c) and (d)) are measured by a F/T sensor attached onto the flange, respectively. Then, the components of $\mathbf{N}$ lying in the plane defined by the rotation axis ($\mathbf{N}_x$ or $\mathbf{N}_y$) is estimated. After each rotation, the robot is moved to align the probe center line $\mathbf{C}$ with the estimated direction.

Desired $\mathbf{N}_x$ is located inside the virtual plane $\mathbb{A}$ that comprises desired $\mathbf{N}$ and the randomly selected axis $\mathbf{x}_{sa}$. Desired $\mathbf{N}_x$ is approximated by $\mathbf{C}$ when the probe is rotated onto the plane $\mathbb{A}$. Theoretically, this is also the posture resulting in ${}^{sa}F_y$ to be zero. Then, the second rotation around the axis $\mathbf{y}_{sa}$ that is orthogonal to $\mathbf{x}_{sa}$ is conducted. It is used to estimate $\mathbf{N}_y$ where ${}^{sa'}F_x$ is reduced to zero. The two rotations around $\mathbf{x}_{sa}$ and $\mathbf{y}_{sa}$ are denoted as X-rotation and Y-rotation, as shown in Fig. 4 (c) and (d).

However, human tissue, such as the human limbs, are not completely rigid. There are some soft tissues (i.e. muscles) between the skin and an underlying bone. In real scenarios, small and unexpected deformations of soft tissues are generated to balance the external force. Thus, the recorded force is affected, particularly, in the applications requiring the applied force to be small. Accordingly, to identify the normal direction of human tissues, the measured forces ${}^{sa}F_y$ and ${}^{sa'}F_x$ (see Fig. 4 (c) and (d)) will not be exactly zero when the US probe is accurately placed along desired direction $\mathbf{N}_x$ or $\mathbf{N}_y$. To address the limitation of the simple threshold-based method, here a model-based optimization method is employed to extract $\mathbf{N}$. As the model-based method estimates the desired direction based on the whole experimental force data rather than on a single value, it is more robust in terms of adapting to the small differences between the ideal and real cases.

B. Mechanical Model

In this subsection, we explain the theoretical mechanical model describing two successive rotations (X-rotation and Y-rotation) with a given contact point. The goal of the mechanical model is to establish a framework that allows understanding the exact relationship between the measurements of the F/T sensor and the tilt angle of a probe. The problem can be decomposed into two independent subproblems. First, $\mathbf{N}_x$ is estimated based on the rotation around $\mathbf{x}_{sa}$. Then, $\mathbf{N}_y$ is computed based on the rotation around $\mathbf{y}_{sa}$, after the X-rotation alignment has been executed.

First, the F/T sensor origin $\mathrm{P_s}$ is projected onto the selected rotation axis $\mathbf{x}_{sa}$ yielding point $\mathrm{P_s'}$. The equivalent radius of X-rotation R_p is equal to the distance between $\mathrm{P_s}$ and $\mathrm{P_s'}$.

$$R_p = \sqrt{|\mathbf{C}|^2 - L_x^2} \tag{2}$$

where $\mathbf{C}$ is the probe length vector (including the length of fixture) from $\mathrm{P_s}$ to the tool center point (TCP) P_{tcp}, and L_x is the distance between $\mathrm{P_s'}$ and P_{tcp}.
After placing the US probe on a given contact point with the random posture, L_x is computed using Eq. (3):

$$L_x = \mathbf{C} \cdot \mathbf{x}_{sa} \tag{3}$$

where $\mathbf{x}_{sa}$ is a unit vector.
Then, a unit vector $\mathbf{z}_{sa}$ that is orthogonal to $\mathbf{x}_{sa}$ is defined in the direction of the equivalent radius R_p as shown in Fig. 4 (c). The unit vector $\mathbf{z}_{sa}$ is calculated using Eq. (4):

$$\mathbf{z}_{sa} = \frac{\mathbf{C} + L_x \cdot \mathbf{x}_{sa}}{|\mathbf{C} + L_x \cdot \mathbf{x}_{sa}|} \tag{4}$$

Accordingly, the Cartesian coordinate frame {sa} corresponding to the randomly selected $\mathbf{x}_{sa}$ is well-defined by $\mathbf{x}_{sa}$, $\mathbf{z}_{sa}$, and $\mathbf{y}_{sa} = \mathbf{z}_{sa} \times \mathbf{x}_{sa}$. The reaction force component in $\mathbf{y}_{sa}$ (${}^{sa}F_y$) is able to be represented by a function with respect to the rotation angle around $\mathbf{x}_{sa}$ (θ_x) from plane A to real-time equivalent radius R_p.

$${}^{sa}F_y = \mathrm{sgn}(\theta_x)\frac{R_p}{|\mathbf{C}|}\ F_c \cdot \tan\theta_x \tag{5}$$

where $\mathrm{sgn}(\theta_{out})$ is the sign function.
The measured ${}^{sa}\hat{F}_y$ is computed based on the recorded force using Eq. (6):

$$\begin{aligned} {}^{sa}\hat{\mathbf{F}}_r &= {}^{sa}_{tcp}\mathbf{R}\ {}^{tcp}_{s}\mathbf{R}\ {}^{s}\mathbf{F}_r \\ {}^{sa}\hat{F}_y &= {}^{sa}\ \mathbf{F}_r(y) \end{aligned} \tag{6}$$

where ${}^{A}_{B}\mathbf{R}$ is the rotation matrix used to describe the frame {B} relatively to frame {A}; ${}^{sa}_{tcp}\mathbf{R} = [{}^{tcp}\mathbf{x}_{sa},\ {}^{tcp}\mathbf{y}_{sa},\ {}^{tcp}\mathbf{z}_{sa}]^{-1}$, ${}^{tcp}_{s}\mathbf{R}$ is fixed after attaching the F/T sensor on the flange.

Upon the successful completion of the X-rotation computation, the probe is placed along the computed $\hat{\mathbf{N}}_x$, which is located at the plane $\mathbb{A}$ in the ideal case. Then, the corresponding Y-rotation around $\mathbf{y}_{sa}$ is executed. To intuitively describe the reaction force with respect to the rotation angle around $\mathbf{y}_{sa}$ (θ_y) ranging from desired $\mathbf{N}_x$ to real-time probe C, the other Cartesian coordinate frame {sa'} can be defined, where $\mathbf{y}_{sa'} = \mathbf{y}_{sa}$, $\mathbf{z}_{sa'} = \mathbf{C}$ and $\mathbf{x}_{sa'} = \mathbf{y}_{sa'} \times \mathbf{z}_{sa'}$ (Fig. 4 (d)). The reaction force component in $\mathbf{x}_{sa'}$ (${}^{sa'}F_x$) is computed using Eq. (7):

$${}^{sa'}F_x = -\mathrm{sgn}(\theta_y)\ F_c \cdot \tan\theta_y \tag{7}$$

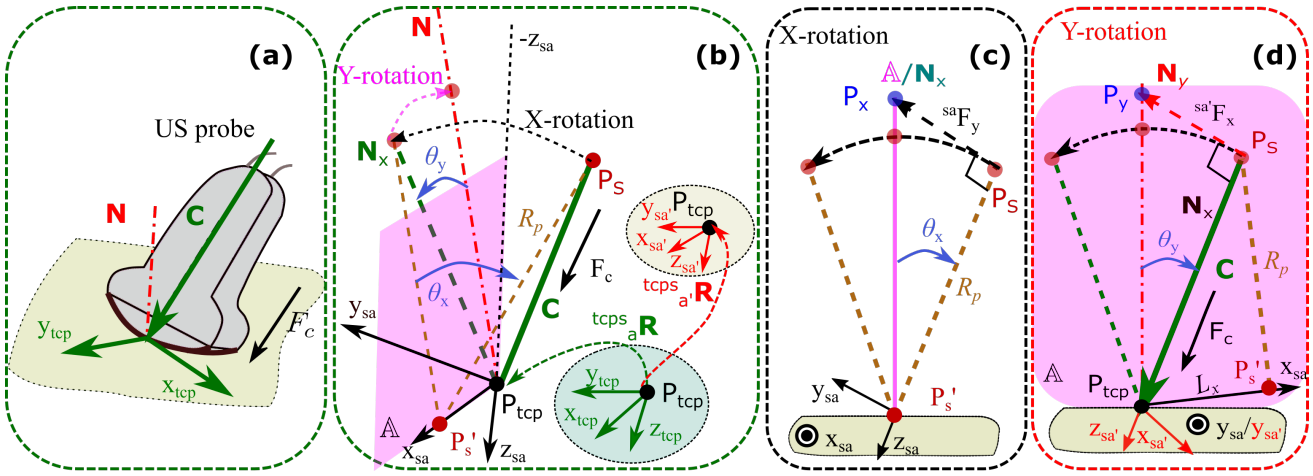

Fig. 4. Theoretical mechanical model of the two successive rotations; (a) a 3D view of a random contact between the convex probe and the unknown constraint surface; (b) the 3D model of two orthogonal searching rotations around random $\mathbf{x}_{sa}$ and corresponding $\mathbf{y}_{sa}$ at a fixed point, respectively; (c) 2D view of the rotation around randomly selected axis $\mathbf{x}_{sa}$; (d) 2D view of the rotation around the computed axis $\mathbf{y}_{sa}$, that is normal to $\mathbf{x}_{sa}$. Desired $\mathbf{N}_x$ is estimated based on the X-rotation. Then the Y-rotation is performed from the estimated $\mathbf{N}_x$. Computed $\mathbf{N}_y$ is used to approximate $\mathbf{N}$ of the unknown constraint surface. P_s and P_{tcp} denote the F/T sensor frame $\{s\}$ and the tool center point (TCP) frame $\{tcp\}$, respectively.

In addition, the measured ${}^{sa'}\hat{F}_x$ during the Y-rotation is calculated based on the sensor output using Eq. (8):

$$\begin{aligned} {}^{sa'}\hat{\mathbf{F}}_r &= {}^{sa'}_{tcp}\mathbf{R}\ {}^{tcp}_{s}\mathbf{R}\ {}^{s}\mathbf{F}_r \\ {}^{sa'}\hat{F}_x &= {}^{sa'}\ \mathbf{F}_r(x) \end{aligned} \tag{8}$$

where ${}^{sa'}_{tcp}\mathbf{R} = [{}^{tcp}\mathbf{x}_{sa'},\ {}^{tcp}\mathbf{y}_{sa'},\ {}^{tcp}\mathbf{z}_{sa'}]^{-1}$.

The reaction force model of searching rotations around a random axis ($\mathbf{x}_{sa}$) is formulated in Eq. (5), and Eq. (7). Since the real-time Cartesian frame {tcp} can be computed based on the robotic kinematic model, it is deemed a suitable candidate to be used as a rotation axis without the need for additional computations. Moreover, since the US probe structure (both linear and convex) is symmetrical around the long axis ($\mathbf{x}_{tcp}$) and short axis ($\mathbf{y}_{tcp}$) (see Fig. 1 and Fig. 7), $\mathbf{x}_{tcp}$ and $\mathbf{y}_{tcp}$ are the center lines of the contact area in two orthogonal directions when the probe is close to the normal direction of the constraint surface. This means that the center contact lines remain unchanged during the process of searching rotations, respectively. The unchanged center line of the contact area indicates that no additional deformation is generated along the rotation axis. Therefore, the two searching rotations can be executed around $\mathbf{x}_{tcp}$ and $\mathbf{y}_{tcp}$ in this study. Then, the theoretical reaction force model defined in Eq. (5) and Eq. (7) can be rewritten as Eq. (9), and Eq. (10) for the orthogonal out-of-plane rotation ($\mathbf{x}_{tcp}$) and in-plane rotation (co-planar with the US image plane, $\mathbf{y}_{tcp}$), respectively.

$${}^{tcp}F_y = \text{sgn}(\theta_{out})\ F_c \cdot \tan\theta_{out} \tag{9}$$

where θ_{out} is the out-of-plane offset angle between $\mathbf{N}$ and $\mathbf{C}$. Here, θ_{out} is identical to θ_x when $\mathbf{x}_{sa} = \mathbf{x}_{tcp}$.

$${}^{tcp}F_x = -\text{sgn}(\theta_{in})\ F_c \cdot \tan\theta_{in} \tag{10}$$

where θ_{in} is the in-plane offset angle between $\mathbf{N}$ and $\mathbf{C}$. Here, θ_{in} is identical to θ_y when $\mathbf{y}_{sa} = \mathbf{y}_{tcp}$.

As a result of comparing Eq. (9) and Eq. (10), it can be seen that both forces corresponding to the out-of-plane and in-plane searching rotations are able to be computed using the general equation described in Eq. (11):

$${}^{tcp}F_i = F_a \cdot \tan\theta_j + F_b \tag{11}$$

where $(i,j) = (y,out)$ or (x,in); F_a and F_b are constant variables for each rotation. Here, F_b is introduced to reduce the negative effect caused by the force bias related to the initial contact condition for the real experimental data.

C. Extracting the Normal Direction

Based on the recorded reaction force ${}^{tcp}\hat{\mathbf{F}}_r$ and the previously derived mechanical model ${}^{tcp}F_i$, $i = x$ or y (see Eq. (11)), a model-based orientation optimization method is proposed to obtain first $\mathbf{N}_o$ and then $\mathbf{N}_i$ as a result of the out-of-plane and in-plane rotation.

However, since the derivative of a tangent monotonically increases until infinity, a small variation in ${}^{tcp}\hat{\mathbf{F}}_r$ may lead to non-negligible errors in a tangent-based fitting result. However, the required maximum angular error in this task is less than $20°$ ($|\theta_i| < 20°$). Therefore, the tangent-based equation (Eq. 11) derived from the theoretical mechanical model can be approximated by a sine-based function applying small-angle approximation ($20° = 0.35$ rad). Compared with the tangent-based equation, the derivative of the sine-based function is limited to the range $[-1, 1]$. Thus, it is more robust to fit the sine-based function to the noise-perturbed ${}^{tcp}\hat{\mathbf{F}}_r$ using Eq. (12):

$${}^{tcp}F_i = p_1^i + p_2^i\ \sin\left(2\pi p_3^i t + p_4^i\right) \tag{12}$$

where $\theta_j = 2\pi p_3^i t + p_4^i$, $(i,j) = (x,out)$ or (y,in), and t is the time stamp of the recorded force data.

The unknown parameters in Eq. (12) are estimated based on the experimental fluctuation-compensated reaction force (FCRF) ${}^{tcp}\hat{\mathbf{F}}_r$ using the constrained non-linear optimization problem described in Eq. (13).

$$min \ \frac{1}{2N}\sum_{j=1}^{N}[{}^{tcp}F_i(j) \ - \ {}^{tcp}\hat{F}_i(j)]^2$$
$$s.t. \begin{cases} 2\pi p_3^i t(k) + p_4^i \le \eta_{max} \\ 2\pi p_3^i t(k) + p_4^i \ge \eta_{min} \end{cases} \quad \forall \ k \in [1, N] \tag{13}$$

where $i = x$ or y; N is the length of ${}^{tcp}\hat{F}_r$; η_{max} and η_{min} are the boundaries limiting the search space, respectively.

Eq. (13) can be solved using the Sequential Quadratic Programming (SQP) method. The desired direction for each of rotations is at $\theta_j = 0$. Therefore, the normal ($\mathbf{N}_o$ or $\mathbf{N}_i$) is approximated by the recorded orientation $\mathbf{R}$ corresponding to the time stamp t_f making $\theta_j = 0$ using Eq. (14).

$$\mathbf{N}_d = \mathbf{R}(t_f) \quad \text{when } \theta_j = 0 \tag{14}$$

The fitted result and the corresponding feature curve used to identify $\mathbf{N}_o$ for an example of the out-of-plane rotation are shown in Fig. 5. Here, an experiment to determine the out-of-plane normal is performed. Then based on the optimized time stamp t_f computed by Eq. (14), the ideal $\mathbf{N}_o$ is approximated by the orientation encoded by the recorded probe orientation $\mathbf{R}(t_f)$. The angular error between the ground truth $\mathbf{N}_o$ and $\mathbf{R}(t_f)$ is 0.7° (error=$\arccos \frac{\mathbf{N}_o \cdot \mathbf{R}(t_f)}{|\mathbf{N}_o| \ |\mathbf{R}(t_f)|}$).

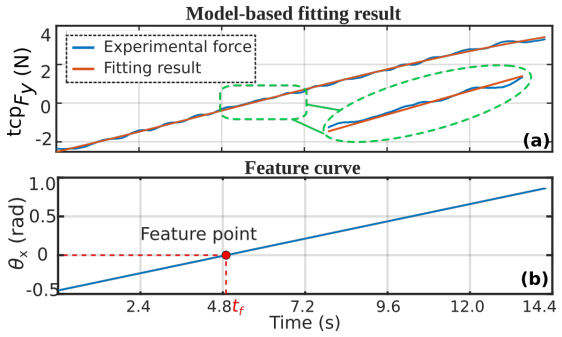

Fig. 5. (a) Fitting result. (b) feature point identification. The experimental force is the denoised force data recorded by F/T sensor. Parameters for the out-of-plane part: rotation range $\theta_{out} \in [10^\circ, -15^\circ]$, phantom tilt angle $\alpha_t = 5^\circ$ and initial in-plane position $\theta_{in} = -10^\circ$.

IV. Control Architecture and Data Processing

In this section, we first describe the control architecture. Then, several de-noising procedures are introduced to mitigate the presence of the large noise in the raw force data recorded during the out-of-plane or in-plane rotations. An overview of the algorithm is shown in Fig. 6.

A. Compliant Control Architecture

The experimental setup for a gel-wax phantom with a planar surface is illustrated in Fig. 7. To measure the interaction force during the estimation of the normal direction $\mathbf{N}$, an F/T sensor was attached to the robotic flange. To validate the proposed method in different cases, a phantom with a flat surface is placed onto the tilted surfaces with varied tilt angles.

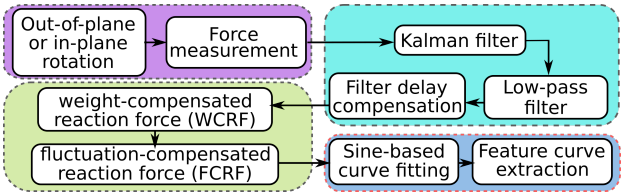

Fig. 6. Workflow of identifying the normal direction based on force measurement.

In addition, since the rotations are performed around $\mathbf{x}_{tcp}$ and $\mathbf{y}_{tcp}$ (frame {tcp}) fixed on the probe, the symbols $\mathbf{N}_x$ and $\mathbf{N}_y$ used in the rotation around an arbitrary frame {sa} are replaced by $\mathbf{N}_o$ and $\mathbf{N}_i$, respectively.

The robot motion is controlled via a 1-DOF compliant controller combined with a 5-DOF position controller as in [14]. The acting 5-DOF position controller is employed to execute the desired scan trajectory or to limit the movement of the contact point around the given position. The compliant controller is applied to exert the constant desired contact force ($\mathbf{F}_d$) between the US probe and tissue aiming to guarantee the US imaging quality and patient safety during screening. The spring-like compliant controller is represented in Eq. (15).

$${}^{tcp}\mathbf{F} = \mathbf{F}_d - \mathbf{K}(\mathbf{P}_i - \mathbf{P}_0) \tag{15}$$

where ${}^{tcp}\mathbf{F} \in \mathbb{R}^m$ is the real force acting onto the contact point in the frame {tcp} (tool center point); $\mathbf{K} \in \mathbb{R}^{m\times 1}$ is the stiffness vector; $\mathbf{P}_0$ is the position where the robot enters force mode; $\mathbf{P}_i$ is the current position.

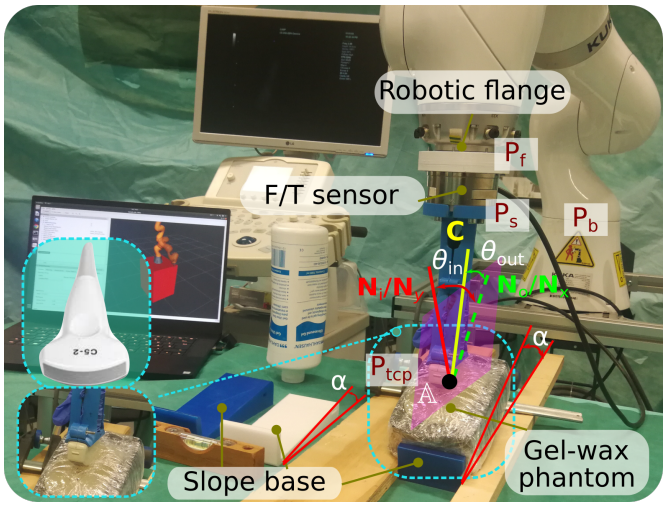

Fig. 7. Experimental setup on the gel-wax phantom. The rotation is performed around $\mathbf{x}_{tcp}$ (out-of-plane view) and $\mathbf{y}_{tcp}$ (in-plane view) rather than the frame {sa} corresponding to an arbitrary axis. The symbols $\mathbf{N}_x$, $\mathbf{N}_y$, θ_x and θ_y in Fig. 4 are replaced with $\mathbf{N}_o$, $\mathbf{N}_i$, θ_{out} and θ_{in}, respectively. P_b, P_f, P_s and P_{tcp} denote the origin coordinates in the robotic base frame $\{b\}$, the robotic flange frame $\{f\}$, the F/T sensor frame $\{s\}$, and TCP frame $\{tcp\}$, respectively. Different slope bases are used to tilt the phantom with different angles ($\alpha_t = 0^\circ, 5^\circ, 10^\circ$ and 15°).

B. Force Calibration using Particle Swarm Optimization

To obtain the true reaction force component (${}^{tcp}F_i$ in Eq. (11)) during the searching rotation, the weight of the US

probe (including fixture) and the preloading force (to mount the sensor on the robot) were identified and then compensated. The ouput from the F/T sensor (${}^s\mathbf{F}_m$) constituted the combined result of the real contact force (${}^s\mathbf{F}_r$), the probe weight (${}^b\mathbf{W}$), and the initial force offsets (${}^s\mathbf{F}_{off}$), including of the sensor bias and the preloading force.

$$ {}^s\mathbf{F}_m = {}^s\mathbf{F}_r + {}^s_b\mathbf{R}\ {}^b\mathbf{W} + {}^s\mathbf{F}_{off} \tag{16}$$

where ${}^s_b\mathbf{R} = {}^{tcp}_s\mathbf{R}^{-1}\ {}^b_{tcp}\mathbf{R}^{-1}$; ${}^{tcp}_s\mathbf{R} = [0\ 1\ 0;\ -1\ 0\ 0;\ 0\ 0\ 1]$ is the rotation matrix from $\{s\}$ to $\{tcp\}$; ${}^b_{tcp}\mathbf{R}$ is the varied transformation mapping data from $\{tcp\}$ to $\{b\}$, which is obtained from the forward kinematics; $\{b\}$ is the robot base frame; $\{s\}$ is the F/T sensor frame.

A particle swarm optimization (PSO) is employed to identify the unknown parameters ${}^b\mathbf{W}$ and ${}^s\mathbf{F}_{off}$ based on the experimentally recorded force data. PSO is an iterative population-based stochastic optimization technique inspired by the foraging behavior of bird flocks [28]. Its main advantages are acceptable performance in terms of finding global optima and its simple implementation [29].

PSO utilizes a group of particles to find an optimal solution by moving the particles around in a search space. The search process is guided by searching for the minimum of the fitness function F_n. In this study, F_n is given by Eq. (17):

$$F_n = \frac{1}{3N}\sum_{i=1}^{N} \|{}^s\mathbf{F}_m(i) - ({}^s_b\mathbf{R}(i){}^b\mathbf{W}(i) - {}^s\mathbf{F}_{off})\| \tag{17}$$

where N is the number of measurements.

C. De-noising and Compensation of Recorded Force

The measured force data contains noise due to the undesired contact conditions and digital noise. Therefore, a set of denoising steps are applied to the measured force data. First, a Kalman filter (KF) is used to remove the Gaussian digital noise caused by the F/T sensor and the robotic servoing system. Following the steps listed in [25], the transition matrices for the estimated state (A) and the measured value (H) of KF are set to be the identity matrix because the last measurement could be set as the predicted value due to the high sampling frequency ($F_s = 83Hz$) of the F/T sensor and the slow rotational velocity (0.025 rad/s). The process and measurement noise model are empirically chosen to be $\mathcal{N}(0, 10^{-4})$ and $\mathcal{N}(0, 10^{-6})$, respectively. The output of KF is shown in Fig. 8.

Since the rotations are non-periodic and executed with slow velocity ($0.025\ rad/s$), the resulting force corresponding to the rotation is mainly distributed in the low-frequency part. Therefore, a low-pass filter is applied to restrain the high-frequency noise. Its stop-band frequency is determined using the fast Fourier transform (FFT). The FFT results of measured force F_m and the corresponding power spectral density (PSD) are shown in Fig. 8 (c). The PSD is rapidly attenuated after $5\ Hz$, and the energy (cumulative PSD) at $5\ Hz$ occupies over 86% of the total signal energy. Hence, the stop-band frequency is set to $5\ Hz$.

However, the signal will experience a constant phase shift (group delay) after applying the low-pass filter. This corresponds to time delay (t_{de}), defined as the derivative of the phase with respect to frequency. More details can be found in [30]. The output data of the low-pass filter are further corrected by shifting the denoised signal by t_{de}. Concerning the general S-tap low-pass filter, t_{de} is calculated using Eq. (18):

$$t_{de} = (S-1)/(2 * F_s) \tag{18}$$

To further extract the force corresponding to the searching rotation from low-pass filter result, the weight of the probe (including fixture) should be compensated. In all experiments, the bias of the force sensor measurement is compensated when the probe is aligned along the ${}^bz$ direction. Then, based on the probe weight (${}^s\mathbf{F}_w$ and ${}^s\mathbf{F}_{off}$) estimated by PSO, the weight-compensated reaction force (WCRF) in frame $\{tcp\}$ (${}^{tcp}\mathbf{F}_r$) is calculated by rewriting Eq. (16) as Eq. (19).

$${}^{tcp}\mathbf{F}_r = {}^{tcp}_s\mathbf{R}({}^s\mathbf{F}_m - {}^s_b\mathbf{R}\ {}^b\mathbf{W} - {}^s\mathbf{F}_{off}) \tag{19}$$

It can be seen in Fig. 8 (b), that the real contact force along $\mathbf{C}$ (${}^{tcp}F_z$) is not exactly equal to the desired F_c, due to inhomogeneous deformations and small slides occuring between the probe and the contact surface. To restrain the influence of small fluctuations of recorded ${}^{tcp}F_z \in (F_c - \Delta F, F_c + \Delta F)$, the average value of ${}^{tcp}F_z$ during the rotation is computed as ${}^{tcp}\overline{F}_z$. Thus, the fluctuation-compensated reaction force (FCRF) ${}^{tcp}\hat{\mathbf{F}}_r = [{}^{tcp}\hat{F}_x, {}^{tcp}\hat{F}_y, {}^{tcp}\hat{F}_z]$ is calculated by mapping the fluctuated ${}^{tcp}F_z$ to ${}^{tcp}\overline{F}_z$ using Eq. 20.

$${}^{tcp}\hat{\mathbf{F}}_r(i) = \frac{{}^{tcp}\overline{F}_z}{{}^{tcp}F_z(i)}\ {}^{tcp}\mathbf{F}(i), \quad \text{if } \frac{{}^{tcp}\overline{F}_z}{{}^{tcp}F_z(i)} < T_1 \tag{20}$$

where ${}^{tcp}\overline{F}_z = \frac{1}{N}\sum_{i=1}^{N} {}^{tcp}F_z(i)$, N is the number of measurements.

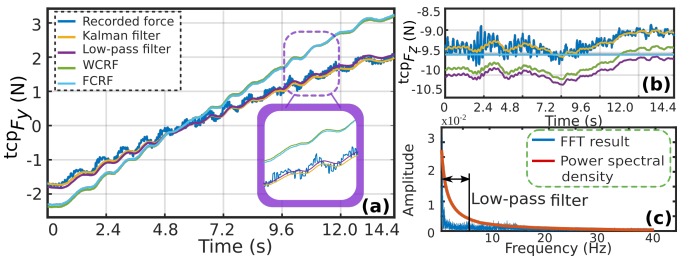

Fig. 8. Effect of the processing steps on the data recorded during the out-of-plane rotation; (a) and (b) display ${}^{tcp}F_y$ and ${}^{tcp}F_z$, respectively; (c) shows the FFT result on ${}^{tcp}F_y$. Experimental parameters: rotation range $[10, -15]°$, the phantom tilt angle $\alpha_t = 5°$, initial orientation $\theta_{in} = -10°$ and $\theta_{out} = -15°$.

V. Results

A. Experimental Setup

The method was evaluated using a KUKA LBR iiwa 7 R800 robot (KUKA Roboter GmbH, Augsburg, Germany), an Ultrasonic Sonix RP machine (BK Ultrasound, Peabody, USA) and a Gamma F/T sensor (ATI Industrial Automation, USA) attached to the end-effector via a custom 3D printed holder. The US B-mode scans were acquired using both a C5-2/60 GPS convex probe and a L14-5/38 GPS linear probe (BK Ultrasound, Peabody, USA).

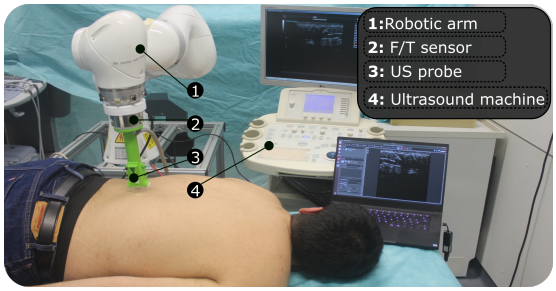

Fig. 9. Experimental setup.

The robot is controlled via a software module based on the Robot Operating System (ROS) framework. The B-mode scans are transferred to a workstation (Intel Core i7-8750H CPU, 16 GB RAM, GeForce GTX 1060) using the OpenIGTLink protocol. The robot's status and force measurements are exchanged at 100 Hz and 83 Hz, respectively. The gel-wax phantom with a flat surface is placed on a flat table. Hence the ground truth is represented by $[0,\ 0,\ 1]$ when $\alpha_t = 0°$. As for the phantom with a non-zero α_t $(5, 10\ and\ 15°)$ and in-vivo volunteer tissues, the ground truth is represented by the normal direction of a local surface composed by three neighbor points distributed around the given position as in [25]. The neighbouring points are manually selected. We have experimentally determined that this method measures the normal with an accuracy of less than $0.1°$ for a gel wax phantom.

B. External Load Calibration Result

The probe weight ${}^b\mathbf{W}$ and the initial force offset ${}^s\mathbf{F}_{off}$ are optimized through minimizing the fitness function F_n (Eq. (17)) using PSO. The parameters of PSO are listed as follows: acceleration constants $c_1 = c_2 = 2$; inertia weight $\xi_{min} = 0.4$ and $\xi_{max} = 0.9$; particle size $J_p = 24$; the maximum number of iterations: 2000. The measured force (${}^s\mathbf{F}_m$) is recorded while the end-effector is rotated around x_{tcp} and y_{tcp} without any external load. Then the weight of the convex probe (${}^b\mathbf{W} = [0\ \ 0\ \ -4.33]$N) and initial force offset (${}^s\mathbf{F}_{off} = [-0.01\ \ 0.04\ \ -4.31]$N) are obtained using PSO. The algorithm terminated after 1400 iterations, returning the final F_n of 0.0022. Repeating the procedures, the probe weight and initial force offset for the linear probe are calculated as follows: ${}^b\mathbf{W} = [0\ \ 0\ \ -3.05]$N) and ${}^s\mathbf{F}_{off} = [-0.03\ \ -0.05\ \ -3.06]$N.

C. Robustness of the Model-Based Identification Algorithm

To validate the robustness of the method aiming to ensure its usability in real applications without any requirements for the knowledge about the constraint surface, a set of out-of-plane rotations with varying initial in-plane angle offsets θ_{in} and different rotation parameters (direction, start angle, and end angle) are executed. All experiments are conducted on the same gel-wax phantom with a flat surface. The phantom is placed on a tilted surface ($\alpha_t = 5°$) (see Fig. 7) to mimic the non-planar human tissues. The resulting angular difference between the estimated normal $\hat{\mathbf{N}}_o$ and actual $\mathbf{N}_o$ are listed in TABLE I.

From Table I, it can be seen that the average angular difference $\bar{e}_{out}$ (mean±SD) summed over all trials is $2.1 \pm 1.5°$. This is smaller than the error of human operators reported in [25], which is $3.2 \pm 1.7°$. Furthermore, in two cases, e_{out} of zero was achieved, and in 51 out of 60 cases (85%), e_{out} was less than three degrees. The two cases with the zero error contain one sample with the largest rotation range ($[-15, 10]$) and one sample with the smallest rotation range ($[-5, 5]$). The average errors for each row and column are denoted by $\bar{e}_{ra}$ and $\bar{e}_{off}$ in the table. It can be seen that there is no significant difference between the experiments conducted using different θ_{in} and θ_{out} values. When grouped by a rotation direction, the average errors $\bar{e}_{out}$ for the forward and backward scanning are $1.9 \pm 1.5°$ and $2.3 \pm 1.5°$, respectively. However, the t-test (wiht the probability $p = 0.27 > 0.05$) yielded that the search direction has no significant impact on the identification result. Therefore, the proposed method demonstrated the capability of providing the sufficiently accurate estimate of $\mathbf{N}_o$ for various θ_{in} and rotation parameters (direction, starting angle, and ending angle).

However, there are three suboptimal cases ($e_{out} \geq 5°$, marked in red in Table I). Two of them occurred when the start or the end of the rotation is close to the desired direction ($\leq 5°$). This is because the US probe is not a mass point as modeled in Fig. 7. This indicates that an asymmetric searching rotation introduces a bias of the measured force data, which is not in line with the theoretical model. However, the largest $\bar{e}_{ra}$ is only $3.4 \pm 1.1°$ when the absolute end angle is $10°$ greater than the absolute start angle ($[5, -15]$). In addition, while starting or stopping the movement of the robotic arm, the motion is not stable during the beginning and ending phases, which will further corrupt the force measurement. This suggests that both start and end points of a rotation had to be sufficiently far from $\mathbf{N}_d$ ($\geq 5°$) to guarantee accurate identification results.

In addition, the impact of the rotation velocity on identification performance is also investigated. Besides $0.025\ rad/s$, three other velocities (0.015, 0.05 and $0.075\ rad/s$) are tested in the experiments using the same frequency for force data acquisition. For each velocity, at least four experiments are repeated under the same condition. The angular error between the detected direction and ground truth slowly grows (0.38 ± 0.23, 0.41 ± 0.28, 0.94 ± 0.40, and $1.40 \pm 0.11°$) as velocity increases from 0.015 to $0.075\ rad/s$. Based on the result, the error behaves close to linear with respect to the velocity. This is because a larger velocity results in larger motion during the same time period. Thus, it is possible to maintain the identification accuracy by increasing the recording frequency of the robot pose and force data when a larger velocity is used.But a slow motion means that the contact condition is closer to the static case while a fast rotation will introduce an unmodeled dynamic contact situation between the probe and human tissue. This means that too high velocity may result in a failure to find a good estimation. Therefore, the rotation velocity should be carefully selected to make a trade-

TABLE I Performance of Model-based Identification method on Tilted Phantom (Mean±SD)

θ_{out} / e_{out} / θ_{in}	Forward Out-of-plane rotation						Backward Out-of-plane rotation						$\bar{e}_{off}$
	[-15, 10]	[-10, 10]	[-5, 10]	[-15, 5]	[-10, 5]	[-5, 5]	[10, -15]	[10, -10]	[10, -5]	[5, -15]	[5, -10]	[5, -5]	
-10	1.0	**0.7**	2.9	2.6	1.5	2.6	2.9	1.7	2.2	2.4	**0.3**	**0**	1.7±1.0
-5	**0**	**7.3**	**0.4**	3.8	3.4	1.9	**0.7**	2.6	2.8	3.7	2.8	2.1	2.6±1.9
0	3.5	**0.4**	2.0	**0.9**	**0.1**	2.2	**0.9**	**0.1**	2.0	2.9	**0.3**	2.0	1.2±1.0
5	3.0	**0.6**	1.4	2.1	3.4	1.7	4.0	4.4	**0.2**	**5.2**	**6.4**	**0.9**	2.8±2.0
10	**0.1**	1.8	**0.6**	1.2	2.0	2.6	2.6	2.8	2.5	2.7	2.5	2.2	2.2±0.7
$\bar{e}_{ra}$	1.5±1.6	2.1±2.9	1.4±1.0	2.1±1.1	2.1±1.4	2.2±0.4	2.2±1.4	2.3±1.6	1.9±1.0	3.4±1.1	2.5±2.5	1.4±1.0	2.1±1.5

*Tilted angle α_t = 5 deg * Units are in deg * **Green**: e_{out}<1.0 deg * **Red**: e_{out}>5.0 deg

off between accuracy and efficiency. If the accuracy is the main concern for a specific application, the probe is suggested to be rotated slowly.

D. Validation on Gel-Wax Phantom

In this section, we systemically describe the performance of the proposed method concerning both convex and linear probes on a gel-wax phantom. To make the experiments more detailed, the phantom is placed on various titled surfaces ($\alpha_t = 0, 5, 10, 15°$). The absolute angular difference for the out-of-plane and in-plane rotations are shown in Fig. 10.

Regarding the out-of-plane experiments, six rotations were executed for each pair of θ_{in} ($-10, -5, 0, 5$ and $10°$) and the probe type (convex and linear). Then, the rotation ranging $[-15, 10°]$ offset from the desired location is performed. Concerning in-plane evaluation, the rotation ranges from $[-13, 8°]$. For each pair of a probe type (linear, convex) and θ_{out} $(-5, 0, 5)$, the rotation is repeated five times. The range of θ_{out} in this case is smaller, as the out of plane alignment is conducted before the in-plane rotation.

From Fig. 10 (a), the average angular difference ($\pm$ SD) for the 120 out-of-plane rotations (e_{out}) is $2.7 \pm 1.9°$ for the convex and $2.5 \pm 1.3°$ for the linear probe. More than 75% of e_{out} for all 240 rotations (both convex and linear probes) are below $3.6°$. As can be seen in Fig. 10 (b), the average in-plane error (e_{in}) is $1.7\pm0.9°$ and $1.0\pm0.7°$ for the convex and linear probes, respectively, based on 60 rotations. The model-based optimization also demonstrates robustness to the various tilt angles α_t used. Due to its flat tip, the proposed method achieves better performance for the linear probe rather than for the convex probe, which contains an arched tip. When considering all 360 rotations (the convex and linear probes, in- and out-of-plane), over 75% of the samples exhibites an error less than $4°$.

It is also noteworthy that although the average error of the in-plane and out-of-plane optimizations are rather close to each other (less than $1°$), the maximum error of the in-plane optimization is much less compared with that of the out-of-plane optimization(convex: $8.5°$ vs $3.3°$; linear: $5.7°$ vs $2.9°$). The differences between the performances of the in-plane and out-of-plane optimizations are caused by the probe structure for which the length in $\mathbf{x}_{tcp}$ is much larger than the width in $\mathbf{y}_{tcp}$ direction. For example, the length and the width of the linear probe are $50\ mm$ and $13\ mm$, respectively. The larger length results in greater force changes when the probe is rotated around the same angle. Thus, the in-plane optimization results are better than those of the out-of-plane optimization as shown in Fig. 10. In addition, the performance differences between the probes (see Fig. 10 (b)) are caused by a similar reason. This is because the linear tip of the linear probe makes it more sensitive to the in-plane rotation compared with the round tip of the convex probe.

In addition, to demonstrate the superiority of the proposed method, we compared it with existing approaches and also human operators as shown in TABLE II. A red cross indicates that a method cannot be applied for the corresponding scenario (e.g. probe type). The performance of the camera based method [10] is computed based on the angular difference between the ground truth and the estimated normal direction of a flat calibration board at different positions and timestamps (90 data in total). In addition, a simple method based on the reaction force ($\mathbf{N} = [\frac{F_x}{|F|}, \frac{F_y}{|F|}, \frac{F_z}{|F|}]$) used in [20], [21] also does not work well in this case, particularly for the linear probe. This is mainly caused by the probe's geometry and the properties of human tissues, which are not as stiff as a workpiece. Since the probe width is much smaller than its length (linear probe: $13\ mm$ vs $50\ mm$), the out-of-plane performance is better than the in-plane performance for both linear and convex probes (see TABLE II).

Then we further compared our proposed method with the state of art probe orientation optimization method [25], which is the first work aimed to fully optimize a US probe orientation (both in-plane and out-of-plane). However, the in-plane optimization method is only applicable to a convex probe and required sufficient amounts of shadows in US images. The force based out-of-plane adjustment was developed based on the searching for an optimized minimum force deviation. In the present study, all available experimental data has been taken into consideration rather than focusing on local minima [25], which makes it more robust to adapt the unmodeled error in real cases (e.g. friction and amount of US gel). The performance of the model-based method is better than that of the local minima based method [25] on a gel-wax phantom ($2.5 \pm 1.3°$ vs $3.1 \pm 1.0°$). Furthermore, the lowest error reported in [25] is $1.7°$ while the best of the out-of-plane orientation achieved by the present work has an error of zero (see Fig. 10 (a)). Based on experiments performed on a phantom, the proposed method outperforms other existing methods, and is comparable to the participating human operators in terms of identification accuracy.

TABLE II Performance of Methods used to Estimate Normal direction on phantom (Accuracy: Mean±SD)

Methods	Convex probe		Linear probe		Samples	Measured signal
	out-of-plane	in-plane	out-of-plane	in-plane		
Human operator [25]	3.2±1.7				60	Human vision and tactile
Huang *et al.* [10]	7.3±3.1#				90	Depth camera image
Reaction force method [20, 21]	5.8±2.2	7.7±2.7	11.2±2.5	15.8±6.9	30/30 30/30	Only force
Jiang *et al.* [25]	3.1±1.0	2.9±0.2	×	×	10/12	Force and US image
Proposed method	2.7±1.9	1.7±0.9	2.5±1.3	1.0±0.7	120/60 120/60	Only force

* Units are in degree. × : method is not appliable. #: Recompute based on RealSense D435.

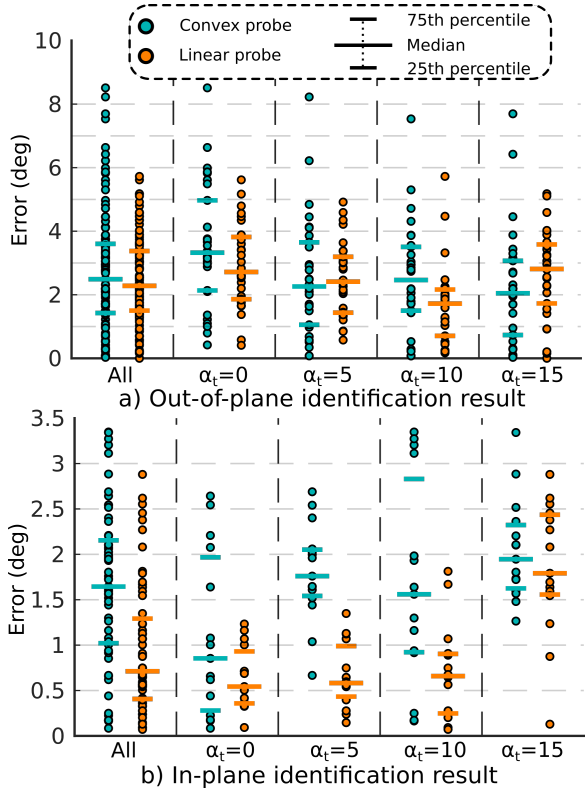

Fig. 10. Absolute angular difference between ground truth $\mathbf{N}_o$ and $\mathbf{N}_i$ and the estimated values $\hat{\mathbf{N}}_o$ and $\hat{\mathbf{N}}_i$ for out-of-plane and in-plane rotation, respectively. The circles represent the absolute angular difference for each experiment, the bar represents the mean value. The bottom and top short bars represent the 25th and 75th percentile, respectively. There are 30 experiments for out-of-plane and 15 for in-plane for each probe type and each α_t. Several initial angular offsets were used ($[-10, -5, 0 - 5, 10]$). Here, α_t denotes the tilt angle of the phantom.

E. In-vivo validation

Since human tissues are more complicated, the impact of the probe orientation on the real US bone images is analyzed as demonstrated in Fig. 11. The radius bone boundary gradually disappears in the US view when the US probe is rotated away from the normal direction of the constraint surface. The bone boundary becomes very weak in the case the tilted angle is over $15°$ as shown in Fig. 11 (d), (e), and (f). Therefore, the probe orientation is deemed important to obtain high-quality US bone imaging for the potential registration between intra-operative US imaging and pre-operative scans (CT or MRI).

To further investigate the performance of the proposed probe orientation adjustment method concerning the real clinical applications, validations were carried out on real human tissues (forearm, upper arm, leg, and back) using the linear probe. To restrain the negative effect caused by breathing, the volunteers are asked to hold their breathing for the experiments on their low back. Ten rotations are executed for each tissue, starting from a random location. The absolute angular error for the in-plane and out-of-plane parts are shown in Fig. 12.

The error corresponding to the various in-vivo tissues ranges from $0.1°$ to $6.0°$. Regarding the out-of-plane rotation, the mean errors (±SD) are $3.7 \pm 1.7°$, $3.1 \pm 1.5°$, $2.5 \pm 1.3°$, and $2.0 \pm 1.8°$ for the forearm, upper arm, leg, and lower back, respectively. This result outperforms that of the previous state-of-the-art approach that was evaluated on a volunteer's forearm, upper arm and back achieved mean (±SD) of $3.7 \pm 1.7°$, $5.3 \pm 1.3°$, $6.9 \pm 3.5°$ [25]. Regarding the in-plane part, the mean errors (±SD) for the same tissues are $2.3 \pm 1.6°$, $3.2 \pm 0.6°$, $2.5 \pm 1.4°$ and $2.3 \pm 1.4°$, respectively. The average errors for the in-vivo tissues are close to the results on the gel-wax phantom. Therefore, we confirmed that the proposed method is partly robust against the distortions caused by unexpected human movement and tissue deformation.

In addition, it is also noteworthy that the best in-plane result on the upper arm ($2.2°$) is worse than the best results on other tissues ($0.2, 0.0,$ and $0.2°$ for forearm, leg, and back, respectively). This is due to the different fat distribution, which makes the upper arm softer than the other tissues. In addition, the round structure of upper arm is more prone to yield sliding between the probe and the tissue, which led to further deterioration of the algorithm accuracy. However, despite these challenges, the worst case in-plane results on the upper arm are still less than $4.0°$.

VI. Conclusion

In the present paper, we introduced a model-based orientation (both in-plane and out-of-plane) optimization method to automatically estimate the normal of an object surface purely based on the measured contact force. This method enables RUSS to automatically obtain US scans with higher quality. The focus of the proposed method is emphasized on the utilization of the underlying mechanical model to obtain a desired direction based on the force values recorded during the two orthogonal fan motions with a certain point of contact. The proposed method is applicable to the most common types of US probes (both convex and linear), and due to its purely force-based nature, it is invariant to image content. Thereby, it could be easily transferred to any robotic system concerning either medical or industrial applications, requiring the estimation of a specific angle between a tool and a contact

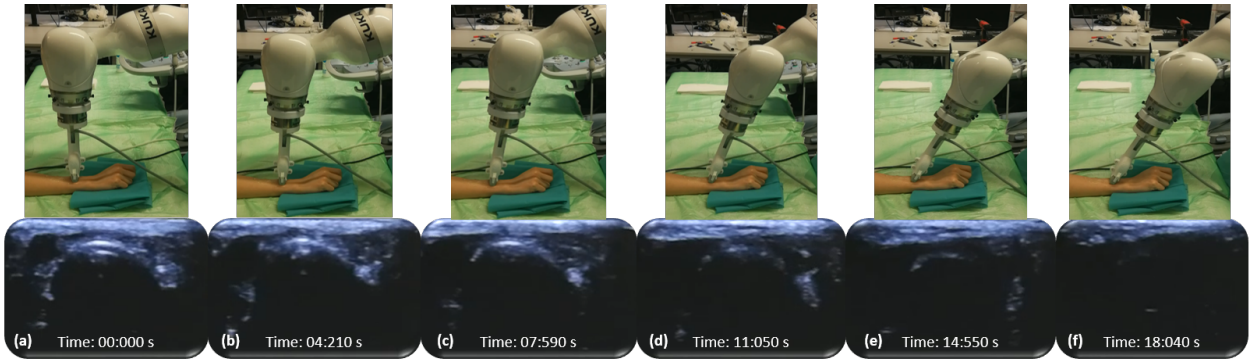

Fig. 11. The impact of the US probe orientation on the US scans of the radius bone. The upper row depicts the probe orientation. The lower row shows the corresponding US images of a volunteer's radius bone. (a), (b), (c), (d), (e), and (f) are the images acquired when the linear probe is titled around $0, 5, 10, 15, 20, 25°$, respectively.

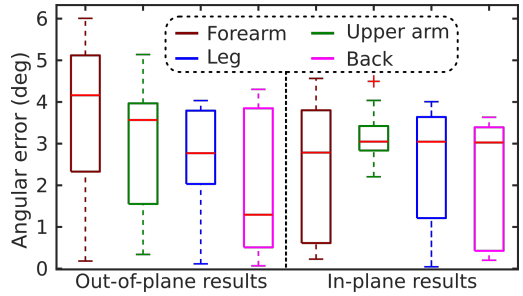

Fig. 12. Absolute errors for the estimation of the desired orientation $\mathbf{N}_d$ on in-vivo tissues.

surface. The performance of the proposed method has been validated both on the gel-wax phantom and on the in-vivo tissue of a human volunteer. Friction is not considered due to the usage of the US gel and the smooth US probe surface resulting in low friction between the scanned tissue and the probe.

Nevertheless, the limitations of the proposed method are also outlined. First, the proposed method was developed for orthopedic applications (e.g. limb) rather than the very soft tissue (e.g. breast) as the contact could severely change the original curvature of soft anatomies, and even the optimal orientation is not necessarily to be normal anymore. Second, if the normal direction of the underlying bone surface is differed considerably from the tissue surface, the orientation optimization procedure had to be performed multiple times at different positions on the scan path.

To conclude, we consider that the proposed approach will contribute significantly into developing novel RUSS for automatic day-to-day clinical examination by enabling the automated adjustment of the probe orientation, thereby achieving better image quality. Future research work will also focus on camera imaging to automatically generate a dynamic scan path and investigate the optimal contact force for different tissues.

REFERENCES

[1] C. M. Court-Brown and B. Caesar, "Epidemiology of adult fractures: a review," *Injury*, vol. 37, no. 8, pp. 691–697, 2006.

[2] M. Ciganovic, F. Ozdemir, F. Pean, P. Fuernstahl, C. Tanner, and O. Goksel, "Registration of 3D freehand ultrasound to a bone model for orthopedic procedures of the forearm," *Int. J. Comput. Assist. Radiol. Surg.*, vol. 13, no. 6, pp. 827–836, 2018.

[3] P. R. Hoskins, K. Martin, and A. Thrush, *Diagnostic ultrasound: physics and equipment*. CRC Press, 2019.

[4] W. Wein, A. Karamalis, A. Baumgartner, and N. Navab, "Automatic bone detection and soft tissue aware ultrasound–CT registration for computer-aided orthopedic surgery," *Int. J. Comput. Assist. Radiol. Surg.*, vol. 10, no. 6, pp. 971–979, 2015.

[5] M. Salehi, R. Prevost, J.-L. Moctezuma, N. Navab, and W. Wein, "Precise ultrasound bone registration with learning-based segmentation and speed of sound calibration," in *Int. Conf. Med. Image Comput. Comput. Assist. Interv. (MICCAI)*. Springer, 2017, pp. 682–690.

[6] M. W. Gilbertson and B. W. Anthony, "Force and position control system for freehand ultrasound," *IEEE Trans. Robot.*, vol. 31, no. 4, pp. 835–849, 2015.

[7] M. L. Balter, A. I. Chen, T. J. Maguire, and M. L. Yarmush, "Adaptive kinematic control of a robotic venipuncture device based on stereo vision, ultrasound, and force guidance," *IEEE Trans. Ind. Electron.*, vol. 64, no. 2, pp. 1626–1635, 2016.

[8] F. Conti, J. Park, and O. Khatib, "Interface design and control strategies for a robot assisted ultrasonic examination system," in *Experimental Robotics*. Springer, 2014, pp. 97–113.

[9] A. Krupa, D. Folio, C. Novales, P. Vieyres, and T. Li, "Robotized tele-echography: an assisting visibility tool to support expert diagnostic," *IEEE Syst. J.*, vol. 10, no. 3, pp. 974–983, 2016.

[10] Q. Huang, B. Wu, J. Lan, and X. Li, "Fully automatic three-dimensional ultrasound imaging based on conventional b-scan," *IEEE Trans. Biomed. Circuits Syst.*, vol. 12, no. 2, pp. 426–436, 2018.

[11] F. Pierrot, E. Dombre, E. Dégoulange, L. Urbain, P. Caron, S. Boudet, J. Gariépy, and J.-L. Mégnien, "Hippocrate: A safe robot arm for medical applications with force feedback," *Med. Image Anal.*, vol. 3, no. 3, pp. 285–300, 1999.

[12] A. Pujas, P. Dauchez, and F. Pierrot, "Hybrid position/force control: task description and control scheme determination for a real implementation," in *in Proc. IEEE/RSJ Int. Conf. Intell. Robots Syst. (IROS)*. IEEE, 1993, pp. 841–846.

[13] T. Yoshikawa and A. Sudou, "Dynamic hybrid position/force control of robot manipulators-on-line estimation of unknown constraint," *IEEE Trans. Robot. Autom.*, vol. 9, no. 2, pp. 220–226, 1993.

[14] O. Zettinig, B. Frisch, S. Virga, M. Esposito, A. Rienmüller, B. Meyer, C. Hennersperger, Y.-M. Ryang, and N. Navab, "3d ultrasound registration-based visual servoing for neurosurgical navigation," *Int. J. Comput. Assist. Radiol. Surg.*, vol. 12, no. 9, pp. 1607–1619, 2017.

[15] B. Ihnatsenka and A. P. Boezaart, "Ultrasound: Basic understanding and learning the language," *Int. J. Shoulder Surg.*, vol. 4, no. 3, p. 55, 2010.

[16] P. R. Hoskins, K. Martin, and A. Thrush, *Diagnostic ultrasound: physics and equipment*.

[17] Y. Han, L. Zhang, M. Guo, C. Fan, and F. Liang, "Tool paths generation strategy for polishing of freeform surface with physically uniform coverage," *Int. J. Adv. Manuf. Technol.*, vol. 95, no. 5, pp. 2125–2144, 2018.

[18] L. Zhang, Y. Han, C. Fan, Y. Tang, and X. Song, "Polishing path planning for physically uniform overlap of polishing ribbons on freeform

surface," *Int. J. Adv. Manuf. Technol.*, vol. 92, no. 9, pp. 4525–4541, 2017.
[19] F. Tian, Z. Li, C. Lv, and G. Liu, "Polishing pressure investigations of robot automatic polishing on curved surfaces," *Int. J. Adv. Manuf. Technol.*, vol. 87, no. 1-4, pp. 639–646, 2016.
[20] J.-P. Merlet, "C-surface applied to the design of an hybrid force-position robot controller," in *in Proc. IEEE Int. Conf. Robot. Autom. (ICRA)*. IEEE, 1987, pp. 1055–1059.
[21] P. Kazanzides, N. S. Bradley, and W. A. Wolovich, "Dual-drive force/velocity control: implementation and experimental results," in *in Proc. IEEE Int. Conf. Robot. Autom. (ICRA)*. IEEE, 1989, pp. 92–93.
[22] P. Chatelain, A. Krupa, and N. Navab, "Confidence-driven control of an ultrasound probe," *IEEE Trans. Robot.*, vol. 33, no. 6, pp. 1410–1424, 2017.
[23] P. Chatelain, A. Krupa, and N. Navab, "Optimization of ultrasound image quality via visual servoing," in *in Proc. IEEE Int. Conf. Robot. Autom. (ICRA)*. IEEE, 2015, pp. 5997–6002.
[24] Q. Huang, J. Lan, and X. Li, "Robotic arm based automatic ultrasound scanning for three-dimensional imaging," *IEEE Trans. Ind. Inform.*, vol. 15, no. 2, pp. 1173–1182, 2018.
[25] Z. Jiang, M. Grimm, M. Zhou, J. Esteban, W. Simson, G. Zahnd, and N. Navab, "Automatic normal positioning of robotic ultrasound probe based only on confidence map optimization and force measurement," *IEEE Robot. Autom. Lett.*, vol. 5, no. 2, pp. 1342–1349, 2020.
[26] J. J. Kaufman and T. A. Einhorn, "Perspectives: Ultrasound assessment of bone," *J. Bone Miner. Res.*, vol. 8, no. 5, pp. 517–525, 1993.
[27] K. Choi, J. L. Kuhn, M. J. Ciarelli, and S. A. Goldstein, "The elastic moduli of human subchondral, trabecular, and cortical bone tissue and the size-dependency of cortical bone modulus," *Journal of biomechanics*, vol. 23, no. 11, pp. 1103–1113, 1990.
[28] J. Kennedy and R. Eberhart, "Particle swarm optimization (pso)," in *Proc. IEEE Int. Conf. on Neural Networks*, 1995, pp. 1942–1948.
[29] Z. Jiang, X. Qi, Y. Sun, Y. Hu, G. Zahnd, and J. Zhang, "Cutting depth monitoring based on milling force for robot-assisted laminectomy," *IEEE Trans. Autom. Sci. Eng.*, 2019.
[30] R. G. Lyons, *Understanding digital signal processing, 3/E*. Pearson Education India, 2004.

Zhongliang Jiang received his M.Eng. degree in Mechanical Engineering from the Harbin Institute of Technology, Shenzhen, China, in 2017. He is currently pursuing the Ph.D. degree in Computer Science at Technical University of Munich, Munich, Germany.

His research interests include medical robotics, robotic learning, and human-robot interaction.

Matthias Grimm received his B.Sc. and M.Sc. in Computer Science from the Technical University of Munich, Munich, Germany, in 2015 and 2018, respectively. He is working towards a Ph.D. in Computer Science at the same university.

His research interests include Image Registration and 3D Reconstruction.

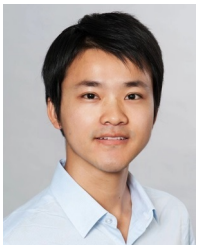

Mingchuan Zhou received Ph.D. degree in computer science from the Technical University of Munich, Munich, Germany, in 2020. He was the visiting scholar at Laboratory for Computational Sensing and Robotics, Johns Hopkins University, USA, 2019. He is currently a postdoc researcher at Chair for Computer Aided Medical Procedures Augmented Reality at the Technical University of Munich.

His research interests include the autonomous system, medical robotics, image processing, and agricultural robotics.

Dr. Zhou was the recipient of Finalist of Best Paper Awards IEEE-ROBIO in 2017.

Ying Hu received her B.Sc. degree from Shanghai Jiaotong University, Shanghai, China, in 1991, and M.Sc. and Ph.D. degrees in mechanical engineering from Harbin Institute of Technology, China, in 1998 and 2007, respectively.

She is currently a professor in the Center for Cognitive Technology, Shenzhen Institutes of Advanced Technology, Chinese Academy of Sciences, Shenzhen. She is the author or coauthor of more than 60 scientific papers published in refereed journals and conference proceedings. Her research interests include parallel robots, medical assistant robots, and mobile robots.

Javier Esteban received his B.Sc degree in Computer Science and M.Sc. in Artificial Intelligence at the University of Salamanca, Spain in 2014 and 2015. He got his second M.Sc. degree in Biomedical Computing at the Technical University of Munich, where now he is working towards his Ph.D.

His research interest include Robotic Ultrasound, Image Registration and Computer Aided Interventions.

Nassir Navab is a Full Professor and Director of the Laboratory for Computer-Aided Medical Procedures at the Technical University of Munich and at Johns Hopkins University. He has also secondary faculty appointments at both affiliated Medical Schools. He completed his PhD at INRIA and University of Paris XI, France, and enjoyed two years of a post-doctoral fellowship at MIT Media Laboratory before joining Siemens Corporate Research (SCR) in 1994. At SCR, he was a distinguished member and received the Siemens Inventor of the Year Award in 2001. He received the SMIT Society Technology award in 2010 for the introduction of Camera Augmented Mobile C-arm and Freehand SPECT technologies, and the '10 years lasting impact award' of IEEE ISMAR in 2015. In 2012, he was elected as a Fellow of the MICCAI Society. He is the author of hundreds of peer-reviewed scientific papers, with more than 36,000 citations and an h-index of 87 as of October 28, 2020. He is the author of more than thirty awarded papers including 11 at MICCAI, 5 at IPCAI, and three at IEEE ISMAR. He is the inventor of 50 granted US patents and more than 50 International ones.